A Finite Element Study of Large Strain Extrusion Machining Using Modified Zerilli–Armstrong Constitutive Relation

Muralimohan Gurusamy
Department of Engineering Design,
Indian Institute of Technology Madras,
Chennai 600036, India
e-mail: muralimohang@alumni.iitm.ac.in

Karthik Palaniappan
Department of Engineering Design,
Indian Institute of Technology Madras,
Chennai 600036, India
e-mail: pkarthik@alumni.iitm.ac.in

H. Murthy
Department of Aerospace Engineering,
Indian Institute of Technology Madras,
Chennai 600036, India
e-mail: mhsn@iitm.ac.in

Balkrishna C. Rao[1]
Department of Engineering Design,
Indian Institute of Technology Madras,
Chennai 600036, India
e-mail: balkrish@iitm.ac.in

The objective of this work is to study the performance of modified Zerilli–Armstrong constitutive relation proposed in our previous study for the finite element modeling of a severe plastic deformation technique called large strain extrusion machining. The modified Zerilli–Armstrong constitutive relation is implemented in a finite element model of large strain extrusion machining of Inconel 718 to analyze the influence of process parameters, i.e., the chip compression ratio and tool–chip friction, on deformation, effective strain distribution, and hydrostatic pressure distribution along the extruded chip. The predicted strain values for different chip compression ratios were validated by comparison with those obtained through an analytical model. The finite element predictions also served as a guideline in designing the large strain extrusion-machining setup on which experiments were conducted to generate Inconel 718 foils with superior mechanical properties. The predicted limits of chip compression ratio were in close agreement with experimentally realizable values. Furthermore, the predicted strain distribution through the thickness of the chip was validated with the results of hardness measurement tests. Microstructural characterization of the Inconel 718 foils was carried out by using both optical and transmission-electron microscopic studies in order to reveal the presence of fine-grain structures. The validations showed the effectiveness of the modified Zerilli–Armstrong constitutive relation in modeling large strain extrusion machining—a variant of the conventional machining process. [DOI: 10.1115/1.4050652]

Keywords: large strain extrusion machining, finite element, Inconel 718, Zerilli–Armstrong, severe plastic deformation, ultrafine-grain

1 Introduction

Severe plastic deformation (SPD) process has emerged as a technique for producing materials with ultrafine-grain (UFG) microstructure and associated enhanced mechanical properties [1–3]. Machining has been demonstrated as an SPD process to produce fine-grain structures in a variety of metals and alloys [4]. Although moderate to large strains can be imposed in a single pass in machining by altering the cutting parameters, it is an unconstrained chip formation process that makes the control of associated dimensions difficult [4]. Large strain extrusion machining (LSEM) is a constrained machining process to overcome the lack of geometric control in chip formation. It affords a simultaneous shape and dimension control through extrusion, in the deformation process for producing UFG chips possessing required bulk-geometry [5]. Moreover, conditions of hydrostatic pressure existing in the deformation zone during LSEM have also been utilized to suppress shear-localization encountered during unconstrained machining of certain metals, e.g., Ti–6Al–4V—a titanium alloy and Mg AZ31B—a magnesium alloy [6]. Therefore, the LSEM process has the ability to subject materials of lower ductility to higher levels of deformation under ambient conditions because of such higher hydrostatic pressures existing in the deformation zone ahead of the tool tip [5].

The LSEM process is carried out at lower cutting speeds to minimize thermal effects and associated coarsening of microstructure during deformation [7,8]. The basic framework of the LSEM process is shown in Fig. 1. A wedge-shaped cutting tool with a positive rake angle (α) removes material from the workpiece at a preset depth of cut (t_0) in the form of a chip with a predetermined thickness (t_c). A constraining tool of a suitable shape is placed at an appropriate position to adjust the thickness of the chip at the stage of its removal from the workpiece. The constraining tool lays flat on the free surface of the workpiece to avoid any buildup of material in the primary shear zone. The extended face of the constraining tool is also held parallel to the rake face of the cutting tool for producing chips with negligible curvature.

De Chiffre [9] originally developed the method of extrusion cutting for producing soft annealed metal strips at higher machining

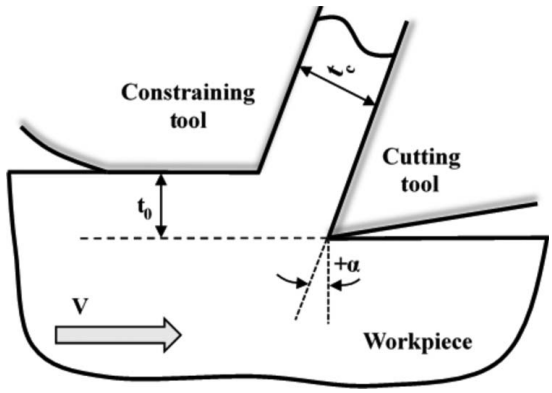

Fig. 1 Schematic of large strain extrusion-machining process

[1]Corresponding author.

Manuscript received October 5, 2020; final manuscript received March 9, 2021; published online April 26, 2021. Assoc. Editor: Jaydeep Karandikar.

speeds. The use of higher cutting speed results in a coarse-grained microstructure because of the associated heating. De Chiffre [9] proposed a simple upper bound model for estimating the effective strain in the chip assuming that deformation is confined only to the primary shear plane which is expressed as

$$\varepsilon = \frac{\gamma}{\sqrt{3}} = \frac{1}{\sqrt{3}}\left(\frac{\lambda}{\cos\alpha} + \frac{1}{\lambda\cos\alpha} - 2\tan\alpha\right) \quad (1)$$

where γ is the shear strain, α is the tool rake angle, and λ is the chip compression ratio defined as t_c/t_o with t_c being the predetermined chip thickness and t_o is the thickness of the uncut chip, as shown in Fig. 1. This equation is identical to the shear plane model for shear strain along the primary deformation zone during conventional machining where the cutting ratio (t_o/t_c) is replaced by the inverse of chip compression ratio ($1/\lambda$) and chip thickness is fixed a priori at t_c [10,11]. The upper bound solution for strain given by Eq. (1) depends only on chip compression ratio and rake angle, and hence, a wide range of strains (1–10), which is one of the main determinants of microstructure and mechanical properties of chip material, can be imposed in the LSEM process through variations of α and λ.

The finite element (FE) modeling of the LSEM process using accurate constitutive behavior will provide a greater understanding of flow mechanisms in the deformation zone. Moreover, the FE models are capable of predicting cutting forces, tool wear, surface integrity, residual stresses, temperature, vibrational displacements, limits for λ and power requirements that are dependent on cutting conditions and hence crucial for producing fine-grained foils through LSEM [12]. Hence, accurate FE predictions will facilitate understanding of deformation mechanics of LSEM along with the designing and optimizing of process conditions aiding setting up of LSEM apparatus with minimal trail experiments.

In this work, the modified Zerilli–Armstrong (ZA) constitutive relation, validated for unconstrained metal cutting in our previous effort, is applied to investigate LSEM, which is a constrained process for generating UFG materials. The predicted effective strain estimates are compared with analytical values, and the influence of tool–chip interfacial friction on imposed strain values was investigated for various chip compression ratios. The implications of FE predictions in conducting LSEM experiments are discussed, and accordingly, FE predictions were utilized in designing process conditions for LSEM to produce UFG foils of Inconel 718. The upper limit of the chip compression is identified by analyzing the FE predictions for the onset of conventional machining where the chip is not thick enough to reach the edge of the constraining tool. Also, the predicted hydrostatic pressure distributions in the deformation zone for various λ values are examined for pressure being less than the flow stress of the work material, which will serve as an indicator for the lower limit of λ realizable for the material. Optical- and transmission-electron microscopy (TEM) studies were conducted to reveal the microstructure refinement occurring during extrusion machining. The confirmation of effective strain distribution through the thicknesses of Inconel 718 foils is also achieved by comparisons with hardness distribution obtained using the micro-indentation technique. This validation also brings out the presence of strain gradient due to flow from the secondary deformation zone adjoining the tool–chip interface. Overall, the demonstration of the usefulness of FE predictions in conducting extrusion-machining experiments further proves the effectiveness of the modified ZA constitutive relation in modeling *severe plastic deformation* processes.

2 Finite Element Analysis of Large Strain Extrusion Machining

The effectiveness of the modified ZA constitutive relationship in the FE modeling of the LSEM process is investigated by carrying out a fully coupled thermomechanical analysis in ABAQUS/Explicit platform [13]. The development of the FE model for the LSEM process is based on the coupled Eulerian–Lagrangian (CEL) method utilized for simulating continuous chip formation during the orthogonal machining process [14–16].

2.1 Geometric Description of Finite Element Model for Large Strain Extrusion Machining. The CEL model of LSEM depicted in Fig. 2 is similar to the model utilized for simulating continuous shear in our previous effort [17] except for the constraining tool. The CEL model has Eulerian boundary conditions defined at left and right edges and the top edge of a predefined chip with spatial constraints. New material is admitted at the inlet of the Eulerian boundary, and properties of the adjacent material are assigned to the new one. The non-Eulerian boundaries are not spatially constrained, and they evolve to their natural shape with the progress of deformation. The solution method adopted here is an arbitrary Lagrangian–Eulerian formulation where FE mesh is neither attached to the material motion (Lagrangian) nor fixed in space (Eulerian), and mesh integrity is preserved by remeshing at equal intervals to prevent element distortion [18].

2.2 Material Behavior and Input Parameters. A new constitutive relation was formulated in our previous study [17] by extending the ZA model of Eq. (2) reported by Samantaray et al. [19] through the inclusion of the athermal stress component as given by Eq. (5). The ZA model proposed by Samantaray et al. [19]

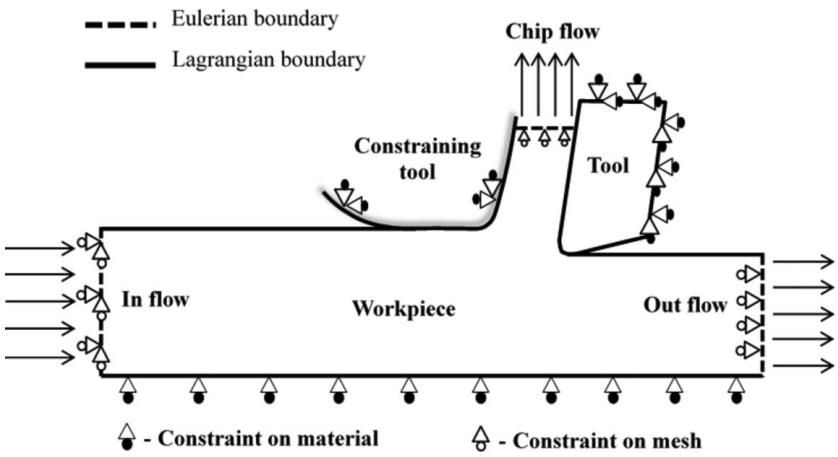

Fig. 2 Schematic illustration of finite element model of LSEM

Table 1 Modified ZA model constants for Inconel 718 [15]

C_0 (MPa)	C_2 (MPa)	n	C_3 (K^{-1})	C_4 (K^{-1})	C_5	C_6 (K^{-1})	T_r (K)	$\dot{\varepsilon}_0$ (s^{-1})
776.15	286.05	0.042	1.25×10^{-3}	-1.823×10^{-4}	0.1505	5.55×10^{-5}	293	1

is given by

$$\sigma = (C_1 + C_2\varepsilon^n) \exp\{-(C_3 + C_4\varepsilon)T^* + (C_5 + C_6T^*) \ln \dot{\varepsilon}^*\} \quad (2)$$

$$T^* = T - T_r \quad (3)$$

$$\dot{\varepsilon}^* = \dot{\varepsilon}/\dot{\varepsilon}_0 \quad (4)$$

where C_1, C_2, C_3, C_4, C_5, C_6, and n are material parameters with C_1 representing the yield stress, C_2 and n are related to strain hardening, C_3 captures the absolute effect of temperature, C_4 represents the coupled effect of strain and temperature, C_5 includes the absolute effect of strain rate, and C_6 describes coupled effect of temperature and strain rate. T_r and $\dot{\varepsilon}_0$ are the reference temperature and equivalent plastic strain rate, respectively.

The ZA model of Eq. (2) does not have an athermal component of flow stress since it is utilized for modeling flow behavior at an elevated temperature while considering strain hardening, strain rate hardening, thermal softening, and the coupled effects of strain and strain rate with temperature. But metal cutting requires both athermal and thermal components for describing the flow stress under a wide range of cutting conditions, and hence, the athermal component was included in Eq. (5) through the parameter C_0. In doing so, the proposed constitutive relation overcomes the inadequacies of popular constitutive models such as Johnson–Cook (JC) and ZA and hence facilitates effective simulation of SPD processes [17]

$$\sigma = C_0 + (C_2\varepsilon^n) \exp\{-(C_3 + C_4\varepsilon)T^* + (C_5 + C_6T^*) \ln \dot{\varepsilon}^*\} \quad (5)$$

Here, the constant C_0 is the athermal component, which is equivalent to the initial yield stress for face centered cubic (FCC) materials [17], and the remaining parameters being the same as in Eq. (2). Table 1 lists the parameters for modified ZA relation validated in our previous effort [17] for Inconel 718 that will be utilized in this paper for LSEM simulations.

The LSEM process is simulated for a cutting tool with a 0-deg rake angle and assumed to remove material from the workpiece at a velocity of 1 m/min for a depth of cut of 250 μm. The cutting speed is kept low to minimize the effects of both temperature and strain rate. The boundary conditions for the FE model also allow for the constraining tool which is assumed to be rigid with no permissible displacements and rotations and the cutting velocity is applied to the inlet Eulerian boundary of the workpiece. The properties of Inconel 718 listed in Table 2 are assigned to the workpiece. The flow stress of the material is temperature-dependent, and hence, a fully coupled thermomechanical analysis is carried out by choosing an appropriate type of element as described in Sec. 2.4 on the FE analysis. The modulus of elasticity, thermal conductivity, and specific heat are assumed constant since their temperature dependence has a negligible effect on finite element predictions [20]. The tool cutting edge has a sufficiently smaller radius of 20 μm ($\leq$1/10 of depth of cut) so as to model a sharp cutting tool [10].

Table 2 Material properties of Inconel 718 at room temperature [20]

Density	Young's modulus	Yield stress	Poisson's ratio	Specific heat	Thermal conductivity
8190 kg/m^3	206 GPa	790 MPa	0.3	435 J/kgK	16.5 W/mK

2.3 Modeling of Friction in Large Strain Extrusion Machining. The friction occurring at the tool–chip interface in machining is a complex phenomenon that has a significant bearing on the chip morphology and also the shear strain associated with chip formation. In this study, the Coulomb friction model with a mean coefficient of friction is assumed over the entire tool–chip contact region. The simulations were carried out with friction-coefficient (μ) values of 0.3 and 0.5 to study the effect of friction on the imposed strain values in the chip. The interface between the constraining tool and chip is assumed to be frictionless as suggested by experimental observations [21] to allow for a smooth transition of the chip through the fixture adapted for performing LSEM. The experimental measurement of strain in chip samples shows that the values are uniform for 80% of the chip thickness and non-uniformity was observed only at the edges on either side for <10% of the chip thickness [21]. Hence, the entire deformation of the work material during the LSEM process is assumed to happen at the shear zone between the cutting tool tip and constraining tool tip [22,23], and accordingly, the interface between the constraining tool and chip is modeled as a frictionless contact. The extended face of the constraining tool which is parallel to the cutting tool helps in producing foils with negligible curvature.

2.4 Mesh Generation and Element Type. The FE model is built from four-node quadrilateral, linearly interpolated, and fully coupled plane-strain elements, CPE4RT, with automatic hourglass control and reduced integration. The minimum size of the element is 10 μm and the maximum being 500 μm. As shown in Fig. 3, the mesh density is finer near the tool tip and becomes coarser away from the primary deformation zone.

Adaptive meshing is used to avoid element distortion. This technique combines features of both Lagrangian and Eulerian analyses, and it applies the relevant analysis where required in the FE model over the course of the simulation [24,25]. The simulation of LSEM has a natural advantage due to geometrical constraints on chip formation that obviates issues associated with unconstrained chip formation where the chip shape continuously evolves until reaching a steady-state [10]. During the simulation of the conventional machining process, the chip shape develops gradually and the mesh associated with the chip will be subjected to distortion and hence will require a large number of remeshings resulting in the increase of computational time and hence resources. In contrast, the chip has a predetermined thickness in LSEM (Fig. 3), which eliminates chip evolution from the incipient stage and thereby negating the problem of mesh distortion.

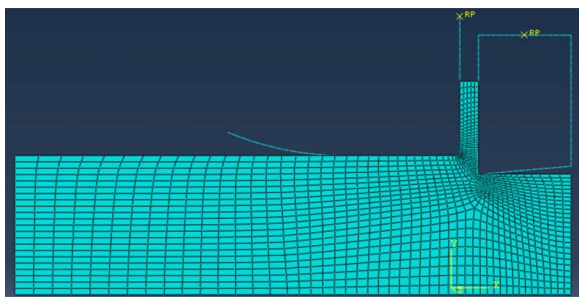

Fig. 3 Finite element mesh generation for the large strain extrusion-machining setup

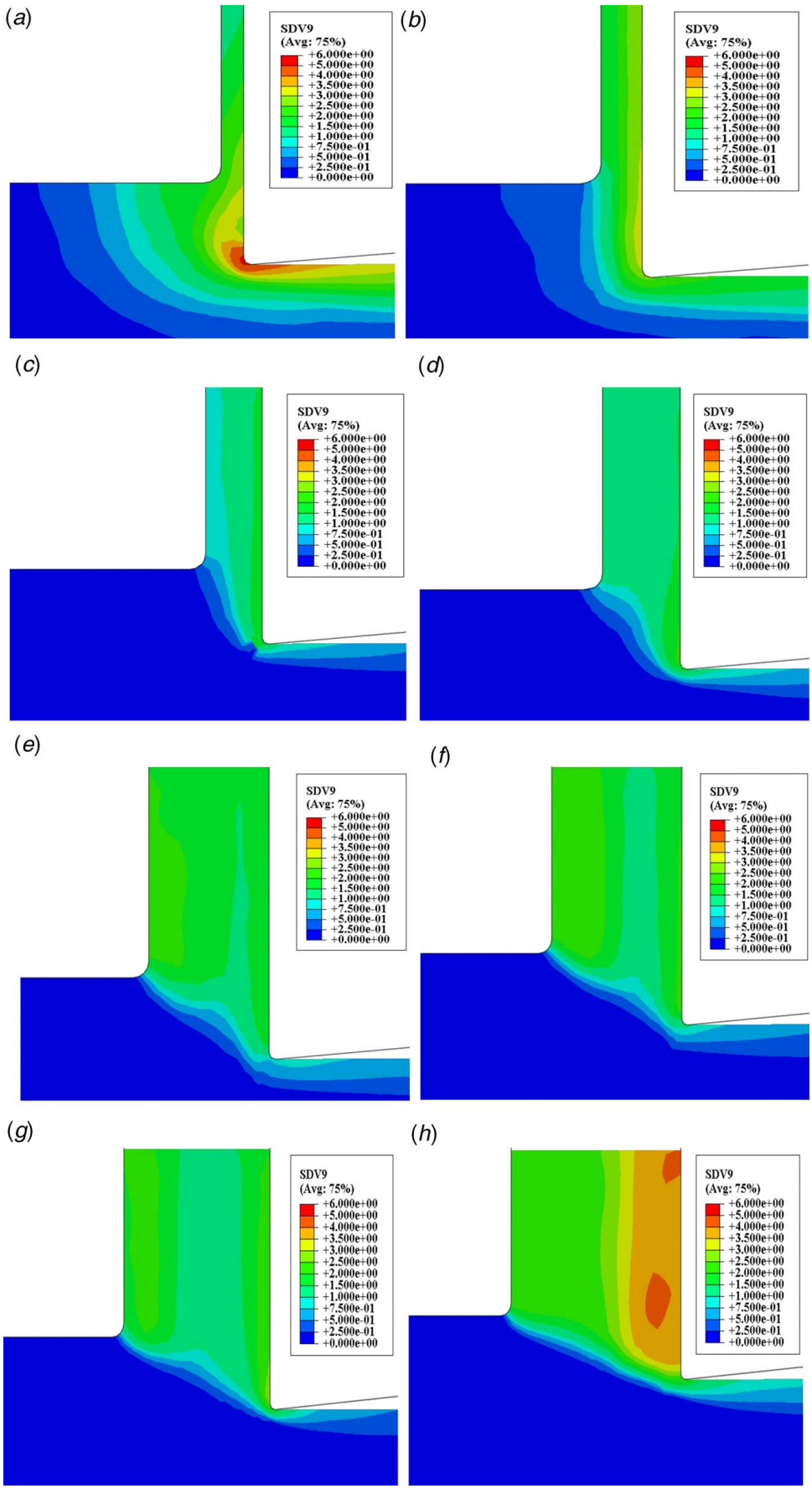

Fig. 4 Predicted effective strain distribution for different λ values at $\mu = 0.3$: (*a*) $\lambda = 0.25$ and $\mu = 0.3$; (*b*) $\lambda = 0.5$ and $\mu = 0.3$; (*c*) $\lambda = 0.75$ and $\mu = 0.3$; (*d*) $\lambda = 1$ and $\mu = 0.3$; (*e*) $\lambda = 1.5$ and $\mu = 0.3$; (*f*) $\lambda = 2$ and $\mu = 0.3$; (*g*) $\lambda = 2.5$ and $\mu = 0.3$; and (*h*) $\lambda = 3$ and $\mu = 0.3$

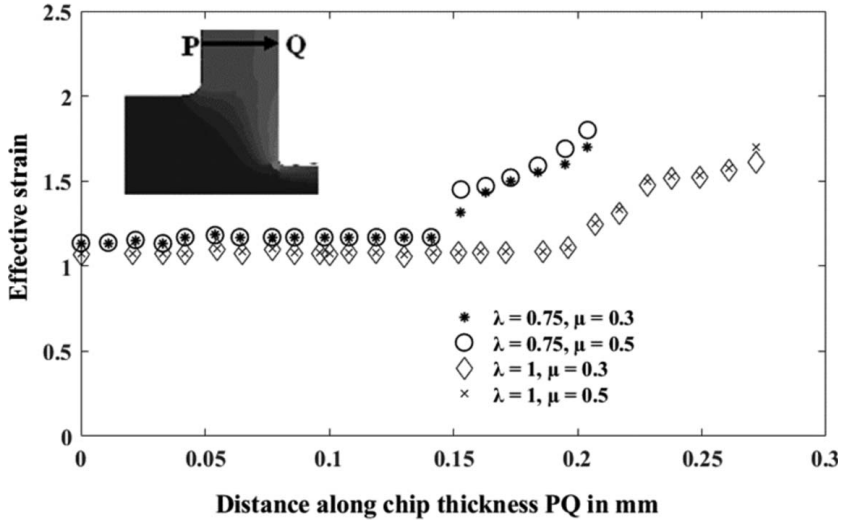

Fig. 5 Effective strain distribution along the thickness of the chip. The labels *P* and *Q* are located on the constraint and rake faces of the chip, respectively.

3 Finite Element Simulation Results

3.1 Strain Distribution. The predicted strain distribution in the chip and workpiece at different chip compression ratios is shown in Fig. 4 for the friction coefficient of 0.3. The amount of strain imposed on the chip varies for different compression ratios, and it has a significant bearing on microstructure refinement achieved through the LSEM process [10]. In a constrained deformation process such as LSEM, the strain distribution is essentially independent of the work material and hence the strain distribution for the nickel-based superalloy, as presented in Fig. 4, is essentially similar to those of lead and copper as reported in the work by Sevier et al. [10].

The predicted effective strain values, through the thickness of the chip, were plotted at uniform intervals between the constraint and rake face for different λ and μ values as shown in Fig. 5. The strain is relatively high but varying in the secondary shear zone adjoining the tool–chip interface. The gradients of strain extend for a smaller fraction of chip thickness, and the strain is essentially constant for the remainder of the chip, as observed in Fig. 5. Hence, the average of the predicted effective strain values over a period of time after reaching a steady-state at the middle of the longitudinal chip section is taken as the representative value for the chip as a whole and is compared with strain calculations made using the upper bound relation of Eq. (1), as shown in Fig. 6. The comparisons show that the predictions for $\mu = 0.3$ matched well quantitatively with the analytical values for different chip compression ratios and accordingly corroborate the predictions of our FE model for the given cutting conditions. Due to frictional effects, the predicted strain at λ values less than 1 for $\mu = 0.5$ does not agree with the analytical model but at $\lambda \geq 1$, the strain values are similar to those at $\mu = 0.3$. The imposed strain of $\varepsilon = 1.08$ is lowest for $\lambda = 1$, and it increases linearly with an increase in λ, limited only by the case of unconstrained machining. For $\lambda = 3$, see Fig. 4(*h*), the predicted strain along constraint edge is considerably lower compared to the cutting tool edge, and $\lambda = 3$ likely marks the onset of unconstrained machining at higher λ values. There is a rapid increase in strain for $\lambda < 1$, and the FE model with the proposed constitutive relation was able to predict the overall trend of imposed strain accurately for different λ values as depicted in Fig. 6. Large values of strain are realized for smaller values of λ, thereby suggesting a higher level of microstructure refinement. Also at smaller λ values, the strain extends underneath the machined surface, as seen in Fig. 4, for $\lambda = 0.25$ and 0.5, which could be exploited for producing UFG microstructure in the machined subsurface for better wear resistance.

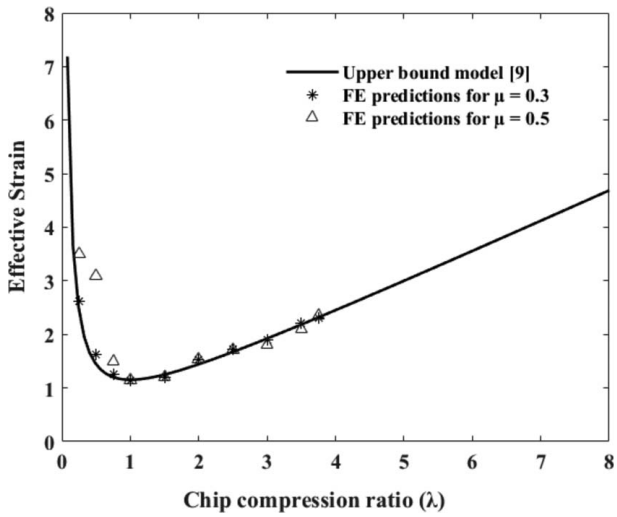

Fig. 6 Variation of effective strain with λ

Because of these fine-grains in the machined surface, there is also a possibility for further refinement in chip microstructure in the subsequent pass during the LSEM process.

3.2 Effect of Tool–Chip Interfacial Friction. In order to study the effect of friction on the effective strain imposed during the LSEM process, FE simulations were conducted with two different μ values of 0.3 and 0.5, as shown in Figs. 4 and 7, respectively. The effective strain values shown in Fig. 4 predicted for various λ values at $\mu = 0.3$ are compared with values shown in Fig. 7 predicted at $\mu = 0.5$ to validate the insignificance of friction as given by the upper bound model of Eq. (1). The secondary shear zone BC, shown in Fig. 7, adjoining the tool–chip interface for $\lambda =$ 0.25, 0.5, 0.75, and 1 experiences a larger strain when compared to the corresponding effective strain distributions at $\mu = 0.3$, shown in Fig. 4. The strain gradient for $\mu = 0.5$ extends only over a smaller portion of the chip thickness producing an increased level of microstructure refinement in this zone. When compared to effective strain distribution at $\mu = 0.3$, there is an increased inhomogeneity of deformation in Fig. 7 as friction intensifies. This effect of friction for λ values less than 1 can be seen only over a smaller region of chip thickness with the remainder of the chip having a

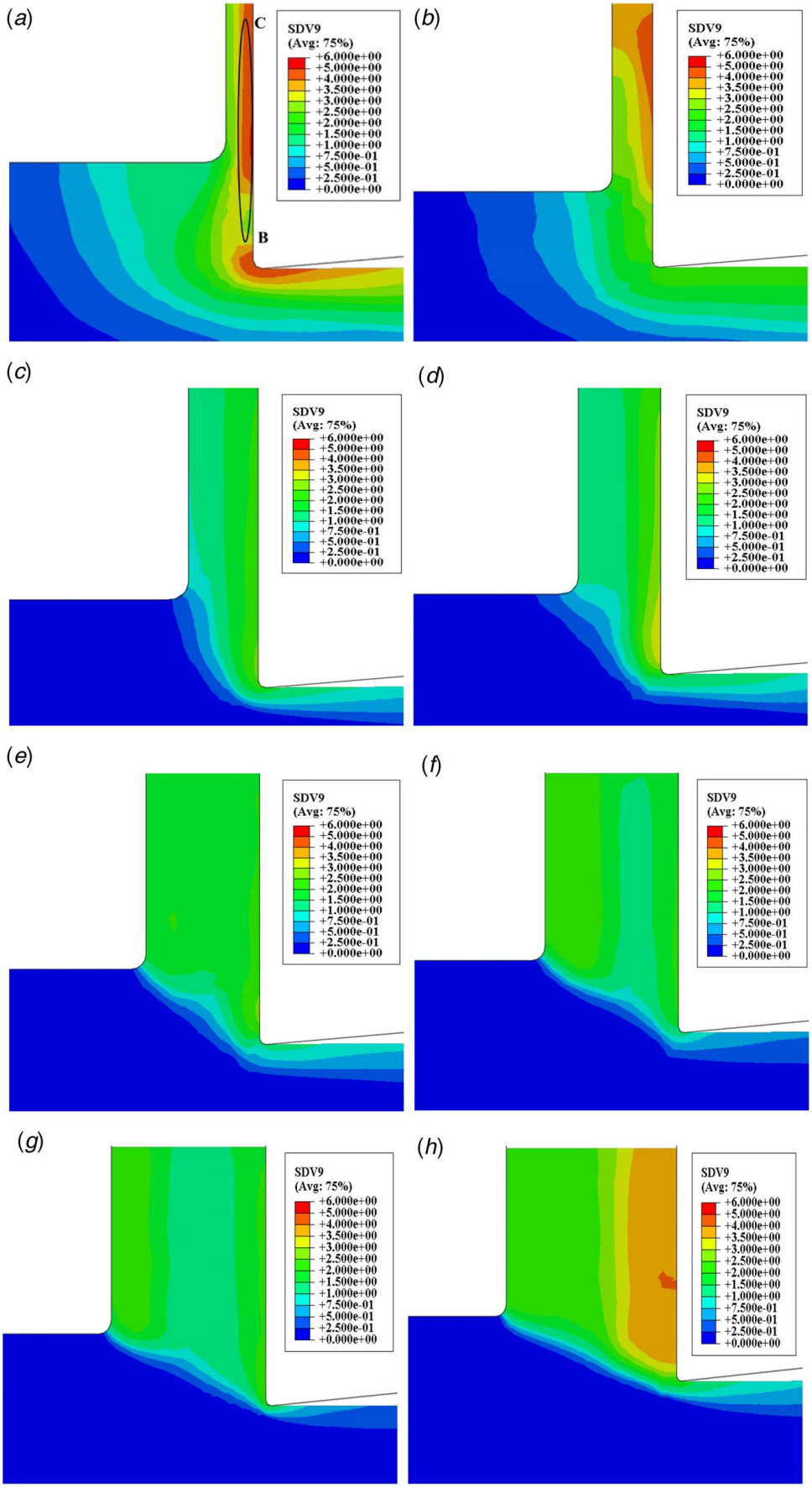

Fig. 7 Prediction of effective strain distribution for different λ values at $\mu = 0.5$: (*a*) $\lambda = 0.25$ and $\mu = 0.5$; (*b*) $\lambda = 0.5$ and $\mu = 0.5$; (*c*) $\lambda = 0.75$ and $\mu = 0.5$; (*d*) $\lambda = 1$ and $\mu = 0.5$; (*e*) $\lambda = 1.5$ and $\mu = 0.5$; (*f*) $\lambda = 2$ and $\mu = 0.5$; (*g*) $\lambda = 2.5$ and $\mu = 0.5$; (*h*) $\lambda = 3$ and $\mu = 0.5$

constant strain similar to strain distribution at $\mu = 0.3$. The effective strain distribution at μ values of 0.3 and 0.5 for higher λ values of 1.5 and 2, as seen in Figs. 4(*e*), 4(*f*), 7(*e*), and 7(*f*), respectively, are identical to that with the absence of any friction. Hence, the imposed strain is primarily controlled by λ and it is independent of material properties and frictional conditions.

3.3 Limits on Chip Compression Ratio. The upper limit on λ corresponds to the onset of conventional machining where the chip is not thick enough for its back surface to reach the constraining tool. A predetermined chip geometry with both surfaces of chip in contact with the cutting- and constraining tool is shown in the FE model of Fig. 8(*a*), corresponding to a time of 0 s and λ of 3.75. As the simulation progresses, the chip gradually evolves (Fig. 8(*b*)) and reaches a steady-state with the final chip thickness being presented in Fig. 8(*c*). For $\lambda = 3.75$, the final chip thickness after reaching steady-state (Fig. 8(*c*)) is smaller than the initial thickness value, and hence, it is not in contact with the constraining tool. This condition shows the onset of conventional machining, and hence, $\lambda = 3.75$ is identified as the upper limit of chip compression ratio. The FE simulations conducted with friction-coefficient values of 0.3 and 0.5 resulted in the same upper limit for λ. Thus, FE simulations can serve in selecting appropriate λ values for the design of the LSEM fixture to impose the proper value of strain on the chip.

3.4 Hydrostatic Pressure Distribution. The hydrostatic pressure distribution helps in identifying the lower limit of λ that is realizable in the LSEM process. The exponential increase in effective strain at smaller λ values coincides with high hydrostatic pressures distributed uniformly throughout the primary deformation zone with maximum values occurring near the surfaces of constraining and cutting tools as shown in Fig. 9. In contrast to effective strain distribution, the hydrostatic pressure distribution depends on material properties [10].

The FE simulations for Inconel 718, as shown in Fig. 9, resulted in larger values of hydrostatic pressure for $\lambda < 2.5$, and these high values in the deformation zone obstruct the flow of chip through the channel between the constraint and cutting tool since they coincide with the flow of workpiece material beneath the cutting tool. The yield stress of the Inconel 718 specimen is 790 MPa as reported in Table 2, and for λ values less than 2.5, the hydrostatic pressure values in the deformation zone are greater than this yield stress. Hence, the λ value of 2.5 will serve as the lower limit that is realizable for the Inconel 718. Large hydrostatic pressures observed at lower values of λ are due to intense deformation of the material under the cutting tool, indicating a transition from machining to simple extrusion with the tool cutting edge serving as one face of the extrusion die [10]. As λ increases, the hydrostatic pressure decreases and becomes less uniformly distributed with high values occurring near the constraining tool edge and being close to zero near the cutting edge for a λ of 2.5 (Fig. 9(*g*)). Hence, a λ of 2.5 should allow for smooth extrusion of the chip between the cutting and constraining tools.

4 Large Strain Extrusion-Machining Experiments

This section describes the execution of LSEM experiments for validating the FE predictions while also generating UFG foils of Inconel 718. Consequently, the predicted limits of chip compression ratio will be validated by comparison with empirically realized values. In addition, the predicted strain gradients along the thickness of the chip will be ascertained using micro-indentation hardness tests. Furthermore, this section will also demonstrate the optimization of process conditions for LSEM through FE simulations. The subsections to follow highlight the setting up of apparatus involving preparation of work material, cutting tool, LSEM fixture, and machining setup utilized for carrying out LSEM.

4.1 Work Material Preparation. The LSEM experiments were performed in an orthogonal setup on plates of Inconel 718

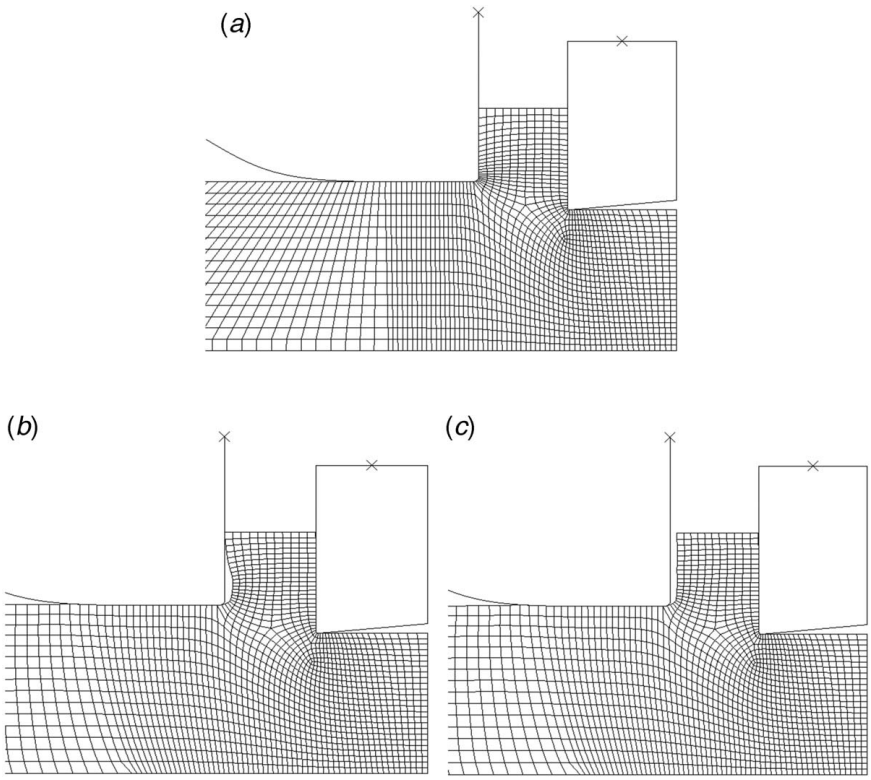

Fig. 8 Onset of conventional machining: (*a*) $t = 0$ s, (*b*) $t = 0.010$ s, and (c) $t = 0.020$ s.

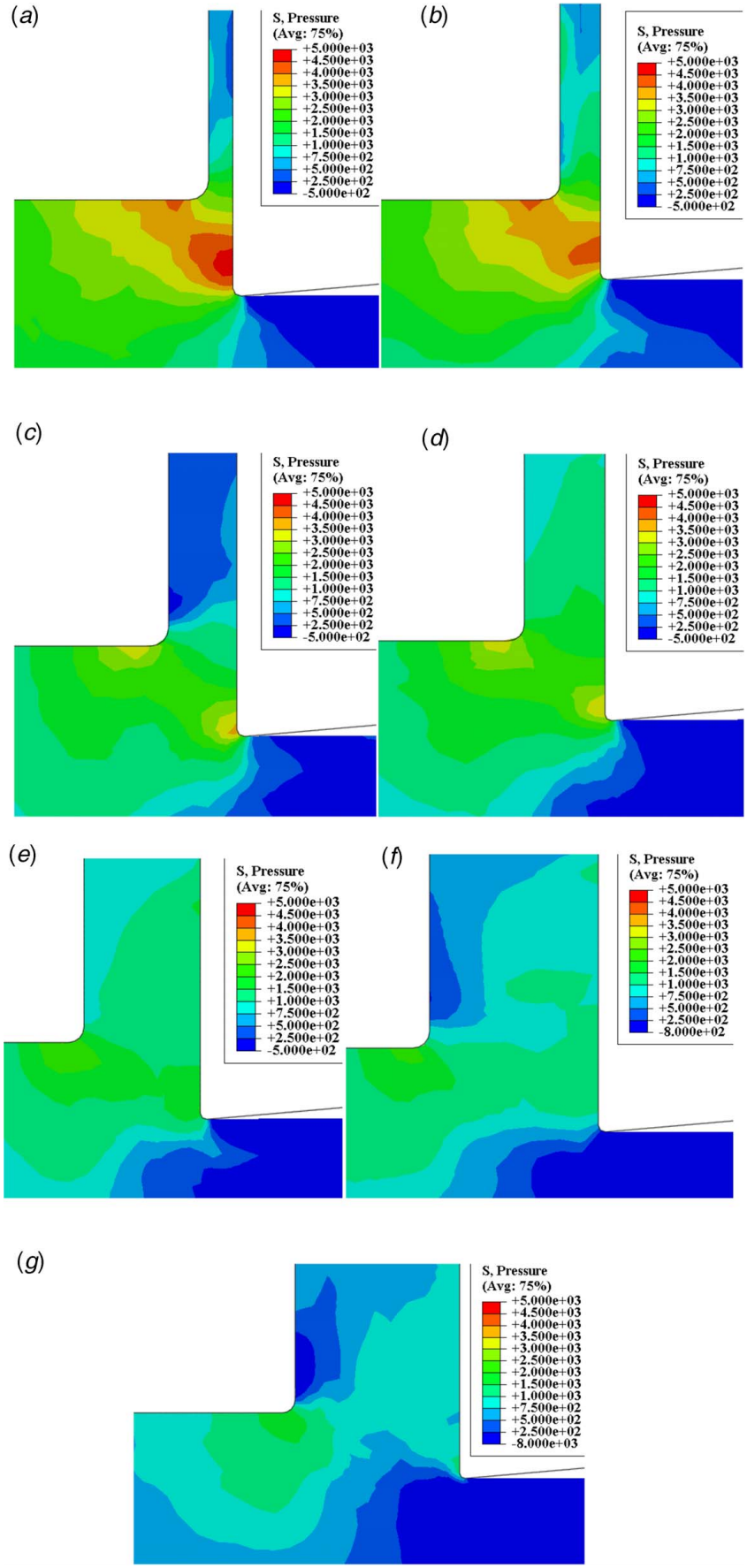

Fig. 9 Hydrostatic pressure (MPa) distribution in the primary deformation zone: (*a*) $\lambda = 0.25$ and $\mu = 0.3$; (*b*) $\lambda = 0.5$ and $\mu = 0.3$; (*c*) $\lambda = 0.75$ and $\mu = 0.3$; (*d*) $\lambda = 1$ and $\mu = 0.3$; (*e*) $\lambda = 1.5$ and $\mu = 0.3$; (*f*) $\lambda = 2$ and $\mu = 0.3$; (*g*) $\lambda = 2.5$ and $\mu = 0.3$

Table 3 Nominal composition of Inconel 718 in wt.%

Ni	Fe	Cr	Nb	Mo	Ti	Al	Co	C	Mn	Si	Ta
50.9	18.7	21.1	4.41	2.85	1.03	0.56	0.207	0.045	0.072	0.06	0.02

Table 4 Heat treatment cycle

Solution treatment :	970 °C for 1 h followed by cooling in air.
Aging:	Aged at 720 °C for 7 h followed by cooling in air.

superalloy. The elemental composition of the as-received material was found by using optical emission spectroscopy (Table 3) in order to verify its chemical composition. The as-received material had a hardness value of 205.8 ± 6.6 HV while the hardness of Inconel 718 utilized for conducting FE simulations corresponds to 340 HV. The as-received material was subjected to the heat treatment procedure given in Table 4 in order to match its hardness with that of the material utilized in the FE analysis. The heat-treated material had a hardness of 325.37 HV ± 9 HV due to precipitation hardening. Subsequently, rectangular plates of Inconel 718 measuring $100 \times 40 \times 3$ mm were extracted from the as-received material by electrical discharge machining (EDM), and these plates were subsequently subjected to the heat treatment cycle of Table 4 before utilizing them for orthogonal LSEM experiments.

4.2 Cutting Tool and LSEM fixture. As shown in Fig. 10(*a*), a restricted-contact single-edge cutting tool designed by Palaniappan et al. [26] was utilized in this study for conducting LSEM experiments on Inconel 718. The cutting tool made of EN8 material is provided with a circular shank so that it can be adapted into the spindle of the computer numerical control (CNC) milling machine and an uncoated tungsten carbide insert (WC–Co) is brazed on to the cutting tool. The chip material is subjected to high temperatures due to friction at the tool–chip interface, which will in turn affect the mechanical properties of the chip during extrusion machining. Hence, in order to reduce the effect of friction, a restricted-contact length of 0.5 mm was provided on the tungsten carbide insert. The cutting tool was also provided with rake and clearance angles of 0 deg and 7 deg, respectively.

The constraint for extruding the Inconel 718 chip from the conventional machining setup is provided by using the fixture, shown in Fig. 10(*b*), developed by Palaniappan et al. [26]. The LSEM fixture made of EN8 material has a slot of dimensions $30 \times 30 \times 26$ mm to hold the cutting tool, and it is held rigidly by Allen screws provided in the LSEM fixture to avoid any relative motion or play during extrusion machining. The hardness of EN8 is less than the chip material, and hence, the inner surface of the groove provided in the fixture got eroded during extrusion because of the intense cutting pressure. Therefore, a tungsten carbide (WC–Co) block of dimensions $12 \times 12 \times 4$ mm is brazed onto the EN8 fixture, as shown in Fig. 10(*b*), to prevent this damage. A wedge-shaped groove of dimensions $5 \times 12 \times 0.375$ mm is cut into this block of tungsten carbide using EDM to allow for the chip to get extruded through the gap leading to extrusion-machining.

The depth of the groove depends on the chip compression ratio, and it is usually identified using a trial-and-error approach, which consumes a significant amount of time and resources [5]. Therefore, in the current study, a time-saving approach using the predicted limits of λ for Inconel 718 realized through the FE analysis were used to identify the depth of the groove. Accordingly, the lower and upper limits of λ forecasted by FE simulations are 2.5 and 3.75, respectively, and these predictions helped in designing the trial experiments. Subsequently, an optimum value of 3.75, allowing smoother extrusion of the chip with lesser thermal effects, was chosen for λ. In order to achieve this λ value, the depth of the groove in the LSEM fixture was selected as 0.375 mm, which is commensurate with a depth of cut of 0.1 mm.

4.3 Experimental Procedure for LSEM. The LSEM experiments were performed on a 5.6 kW HAAS CNC mini mill using heat-treated Inconel 718 plates of dimensions $100 \times 40 \times 3$ mm. The cutting speed was maintained at a low value of 1 m/min. The experiments were performed in the form of linear cutting as depicted in Fig. 11 by restricting the rotary motion of the spindle of the milling machine. The single-edge cutting tool was fed orthogonally against the moving workpiece at a preset depth (t_o) and width (b) of cut, while removing material in the form of a chip. The orthogonality in the extrusion-machining process was achieved by aligning the edge of the cutting tool perpendicular to cutting velocity [26]. Plane-strain conditions were also ensured by choosing a depth of cut of 0.1 mm which is much smaller than the width of cut of 3 mm, i.e., $w/t_o \geq 10$ [27].

5 Experimental Results and Discussion

5.1 Identification of Chip Compression Ratio. The chip compression ratio, which allows for smooth extrusion and also imposes maximum strain, is chosen as the optimum λ value

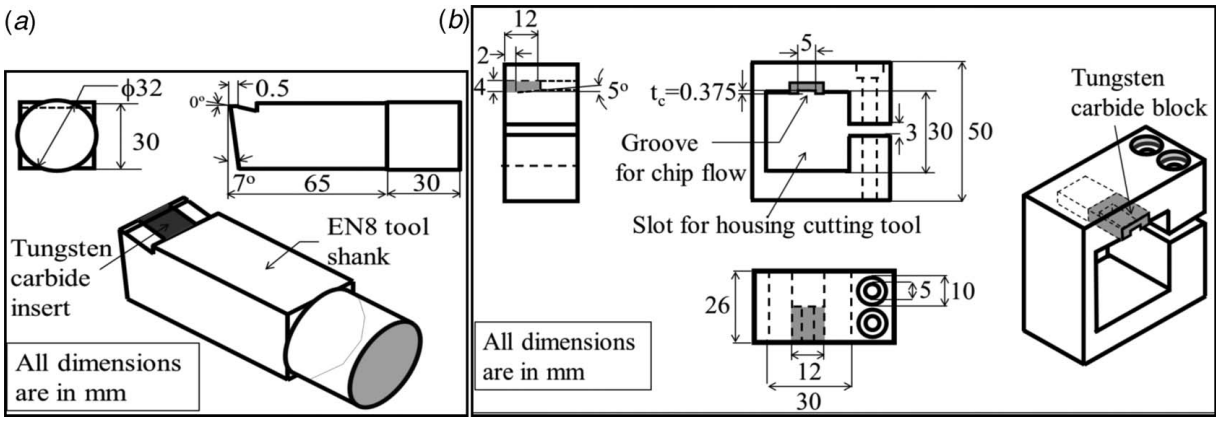

Fig. 10 Schematic of the cutting tool and fixture for implementing LSEM [26]: (*a*) restricted-contact single-edge cutting tool and (*b*) LSEM fixture

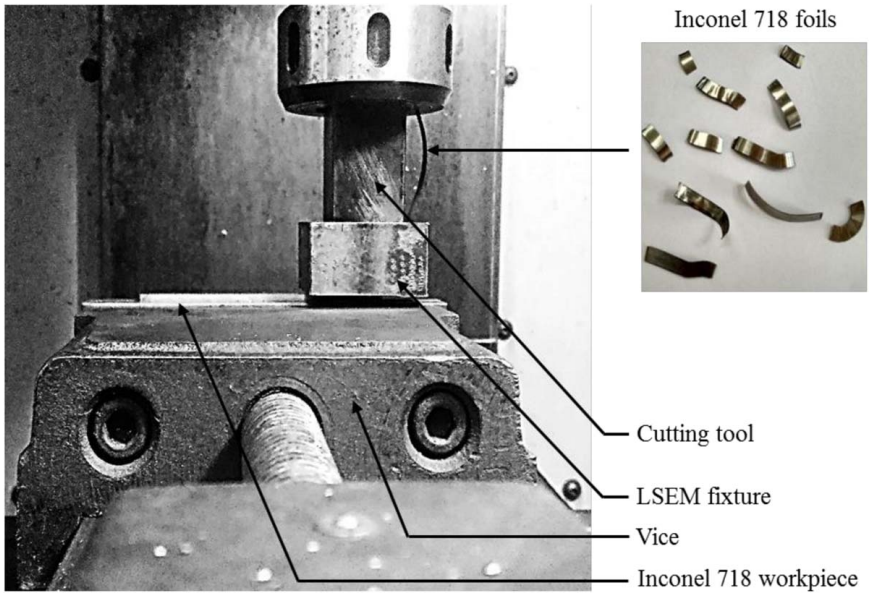

Fig. 11 The HAAS milling machine setup with cutting tool, LSEM fixture, and workpiece [26]. Also shown in the inset are Inconel 718 foils from LSEM.

which influences the depth of groove to be provided in the LSEM fixture. The limits of λ realizable for the given material during extrusion-machining are crucial for the effective design of the LSEM fixture. In literature, these limits were identified by conducting a large number of experiments at different λ values [5]. In contrast, FE simulations carried out in the current study have predicted the limits of λ realizable for Inconel 718 whose LSEM-experimental results in turn were validated again with FE simulations. In subsecs. 3.3 and 3.4, the predicted upper and lower limits of λ were shown to be 3.75 and 2.5, respectively.

The LSEM experiments were conducted at $\lambda = 3.75$ and 4. It was noticed that chips were able to extrude through the fixture for λ of 3.75. However, for λ of 4, a case of unconstrained machining was observed with chip thickness being smaller than the depth of groove provided in the LSEM fixture. Hence, the upper limit of λ has been taken as 4 and the number of trial experiments conducted to identify the same has got drastically reduced because of FE predictions serving as a guideline. The chip was observed to get clogged in the gap resulting between the fixture and cutting tool for experiments conducted at λ less than 3 because of intense hydrostatic pressure experienced by chip between tool rake face and constraint. Therefore, the lower limit of λ was found to be 3 for the extrusion-machining of Inconel 718 with the predicted upper limit having an error of 6% with respect to experimental observations while predictions of lower limit having an error of 17%. A higher λ value of 3.75 was chosen considering the upper and lower limits of 4 and 3, respectively, for reducing energy dissipation in the form of heat and thereby limiting the effect of temperature on the microstructure of resulting foils. This, in turn, also reduces pressure for facilitating a smooth extrusion of the chip through the fixture. Thus, by reducing the number of trial experiments required to identify an optimum value for λ, FE simulations help in saving significant amounts of time and resources associated with LSEM experiments.

Inconel 718 is a difficult-to-machine material because of its special characteristics such as high strength at elevated temperatures, tendency to work harden, poor thermal conductivity, the presence of various precipitates, and hard carbides in its microstructure and high chemical reactivity with tool materials and coatings. These superior properties actually hindered the smooth extrusion of the Inconel 718 chip during experiments with the tungsten carbide insert wearing rapidly in three to four passes while generating a couple of foils. Hence, LSEM experiments on Inconel 718 are fraught with issues of tool wear even at optimum λ value, thereby lowering the process-productivity. Some of the raw LSEM foils obtained from experiments are shown in Fig. 11.

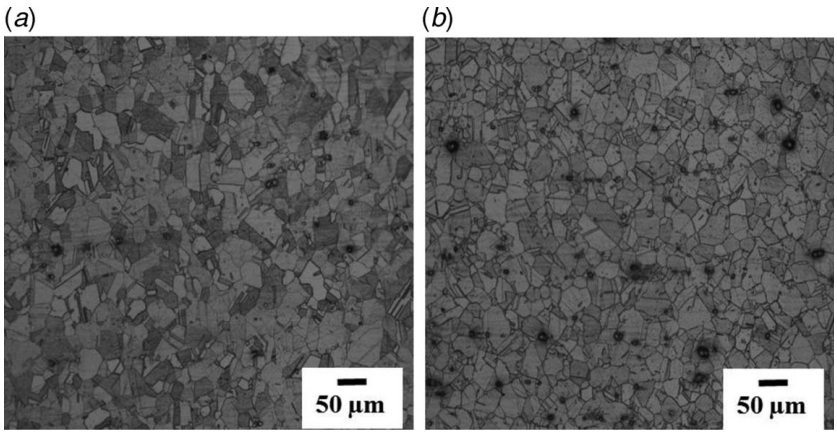

Fig. 12 Microstructure of Inconel 718: (*a*) as received and (*b*) heat treated—precipitation hardened

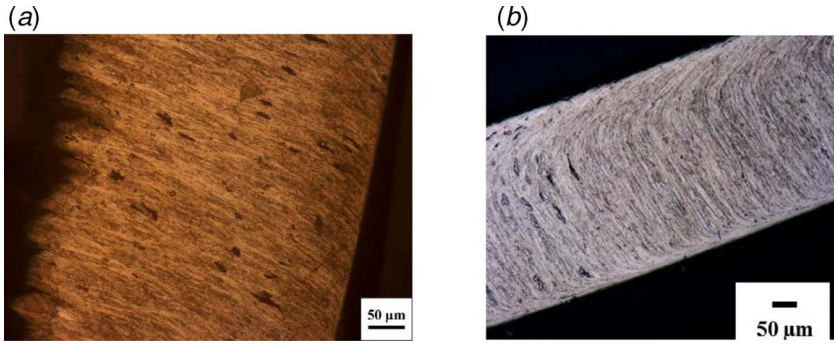

Fig. 13 Optical micrographs of Inconel 718 chips and foils: (*a*) chip from conventional machining and (*b*) foil from LSEM, compression ratio = 3.75

5.2 Optical Microscopy and Hardness Tests. Metallographic studies were carried out for samples extracted from the as-received and heat-treated Inconel 718 plates and also for chip and foil samples obtained from unconstrained and constrained machining of heat-treated workpieces. These samples were mounted in epoxy molds for further polishing. They were successively polished using silicon carbide (SiC)-impregnated emery sheets of different sizes while copious amounts of water were used to remove both heat and debris. Fine polishing was done using alumina powder of size 1500 μm followed by colloidal silica of size 0.08 μm. Kalling's reagent with 5 g copper (II) chloride, 100 ml hydrochloric acid, and 100 ml ethanol was used as the etchant for Inconel 718. The polished samples were etched by immersing in Kalling's reagent for 10 min to reveal microstructures that were captured using optical microscopy.

The Inconel 718 alloy is characterized by a matrix, comprising γ phase of Ni with a face-centered cubic structure, in which precipitate three intermetallic phases, namely, γ' composed of Ni_3 (Al and Ti) with a face-centered cubic structure, γ'' composed of Ni_3Nb with a body-centered tetragonal structure and δ composed of Ni_3Nb with an orthorhombic structure. In addition to various precipitates, it also has niobium-rich primary (interdendritic) metal-carbon (MC)-type carbides with Ti, Mo, and Nb for grain boundary strengthening at elevated temperatures. The precipitation of γ' and γ'' phases occurs between 600 °C and 900 °C [28] that get distributed as fine particles forming the basis for precipitation hardening of this alloy. The microstructures of as-received and aged samples are shown in Fig. 12 with the heat-treated and precipitation-hardened type exhibiting a higher hardness value of 325.37 ± 9 HV vis-à-vis a value of 205.8 ± 6.6 HV for as-received material.

A continuous chip morphology was observed during unconstrained machining of heat-treated Inconel 718 plates as shown in Fig. 13(*a*). The free surface of the chip obtained from unconstrained machining process has wavy, uneven geometry. In contrast, the LSEM process exhibits control over shape and dimension in creating foils as shown in Fig. 13(*b*) where the free surface of the foil does not show any undulations. UFG microstructure developed due to large strains imposed during both unconstrained and extrusion-machining processes are observed in the optical micrographs obtained from the longitudinal section of the chip and foil.

Vicker's indentation technique was used for carrying out hardness measurements on the polished specimens. A minimum of 20 indentations were made on each sample. The hardness of the chip and foil obtained from the aged work material through unconstrained and constrained machining were found to be 518 ± 7 HV and 522 ± 8 HV, respectively. Table 5 also lists the hardness of the bulk, chip, and foil for the aged Inconel 718 alloy. There is a substantial increase in hardness of the foil compared to the bulk (~62%) because of the UFG microstructure formed due to extrusion-machining process. Though similar hardness values are observed between the chip and foil, LSEM helps in controlling geometry and hence creates samples in the form of plates and foils while possessing UFG microstructure. Furthermore, the LSEM process, because of its constrained nature, allows for control of strain and the resulting microstructure by varying only the extrusion ratio for a given tool rake angle. Moreover, the strain imposed on the chip through LSEM can be estimated a priori [5,7].

The predicted effective strain distribution, shown in Fig. 5 and plotted along the thickness direction of foil between the constraint and rake face, was validated by examining variation in hardness, which was measured using Vicker's micro-indentation technique. The effective distribution is compared with the hardness distribution since the hardness varies depending upon the microstructure refinement exerted by the amount of strain imposed during the process. A typical array of micro-indentations made on Inconel 718 foil is shown in Fig. 14, and Vicker's hardness values were accordingly measured at various locations along the thickness of the foil. In order to confirm repeatability, the single array of indentations from *A* to *F* were repeated at 20 different locations along the length of the chip. Figure 15 and Table 6 present the distribution of

Table 5 Vicker's hardness values for different forms of Inconel 718 alloy

Material condition	Bulk	Chip	Foil
Aged	325 ± 9 HV	518 ± 7 HV	522 ± 8 HV

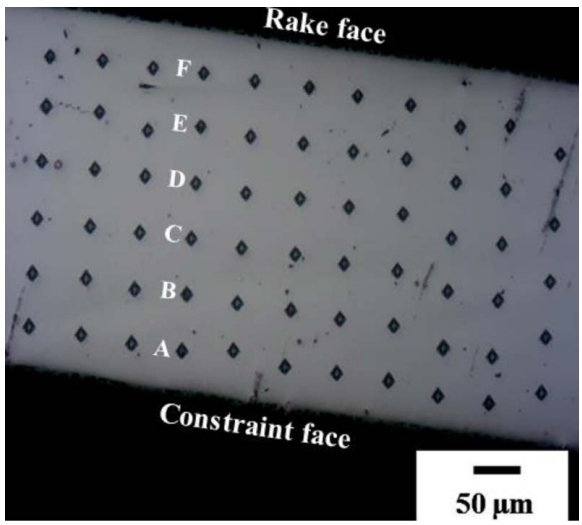

Fig. 14 Inconel 718 foil with an array of micro-indentations for assessment of hardness variation. Indentation load is 50 g.

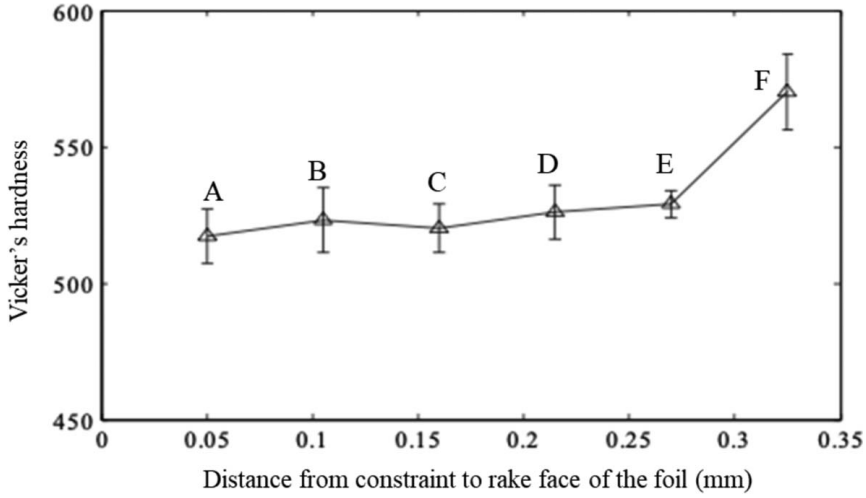

Fig. 15 Vicker's hardness of Inconel 718 foil as a function of distance along its thickness

Table 6 Distribution of Vicker's hardness through the thickness of Inconel 718 foil

Location along the foil thickness	A	B	C	D	E	F
Vicker's hardness (HV)	517 ± 10	523 ± 12	520 ± 9	526 ± 10	529 ± 5	570 ± 14

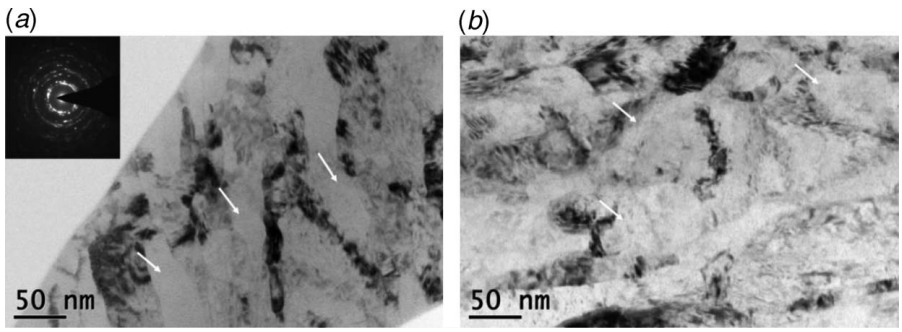

Fig. 16 TEM micrograph and SAD pattern (inset) of Inconel 718 subjected to LSEM. The arrows indicate the presence of elongated and equiaxed grains in (*a*) and (*b*), respectively: (*a*) elongated grains and (*b*) equiaxed grains.

hardness values along the thickness of the foil, which has a similar trend compared to the effective strain distribution of Fig. 5. It can be seen from Fig. 15 that the hardness value is nearly constant for more than half of the chip thickness from the constraint face, and thereupon an increase in value is observed toward the rake face because of increasing microstructure refinement. Such refinement is affected due to large values of strain imposed in the secondary shear zone adjoining the tool–chip interface. Thus, the predicted strain gradient arising due to secondary shear was confirmed through the observation of relatively high and varying microhardness values close to the rake face of the foil as shown in Fig. 15. The shearing effect observed due to friction along both edges of the foil shown in Fig. 13 does not get captured in the hardness distribution of Fig. 15, which might be due to the indentations being away from the shear zone of smaller thickness along the constraint tool face.

5.3 Transmission-Electron Microscopy. The foils were also subjected to electron microscopy to reveal the presence of fine-grain structures formed due to refinement occurring during extrusion-machining. TEM required circular samples of 3 mm diameter that were punched out from the foils and subsequently thinned down to less than 100 μm in thickness by polishing using silicon impregnated emery paper. The thicknesses of the disks were reduced to below 100 μm to ensure the flatness of the sample. The disk sample was made electron transparent by subjecting it to ion milling for about 7 h. The electron transparent disk specimen was then loaded into "TECNAI T20 TEM" (FEI Company, Hillsboro, Oregon) instrument operating at 200 kV. As shown in Fig. 16, the TEM micrographs of Inconel 718 foil reveal the presence of both elongated and equiaxed grains that are typically ~100 nm in size due to the microstructure refinement imposed during extrusion-machining. The selected area diffraction (SAD) pattern shown in the inset of Fig. 16(*a*) indicates a concentric ring-like pattern around a central spot which also attests to the presence of significantly misoriented grain and sub-grain structures.

6 Conclusion

In this study, a finite element model of large strain extrusion machining of Inconel 718 is described, whose behavior is simulated using the modified Zerilli–Armstrong constitutive model. A coupled Eulerian–Lagrangian model was applied to simulate the large strain extrusion-machining process. The finite element

simulation provided good estimates of strain with less than 7% error when compared to analytical values, for variation in chip compression ratio. A series of simulations were carried out with two different friction coefficients along the tool–chip interface for various λ values to describe the effect of friction on imposed strain in the extrusion-machining process. The results show that variation in friction does not have an appreciable effect on strain except along the smaller area adjoining the tool–chip interface.

The finite element prediction of the limits of chip compression ratio realizable for Inconel 718 was in good agreement with those identified through extrusion-machining experiments with an error of 6% and 17% for the upper and lower limits, respectively. The predicted limits for λ also facilitated a reduction in the number of trial experiments required for identifying its optimum value. Thus, finite element predictions of strain, limits of chip compression ratio, hydrostatic pressure distribution, and effect of tool–chip interfacial friction helped in facilitating design and fabrication of the large strain extrusion-machining setup. Accordingly, foils of Inconel 718 with ultrafine-grain microstructure were generated through extrusion-machining experiments, and these foils had a 62% increase in hardness when compared to the aged bulk because of the microstructure refinement afforded by the process.

Optical and transmission-electron microscopy studies were carried out to confirm the presence of ultrafine-grain in the foils. Furthermore, the predicted strain gradients emerging from the secondary deformation zone were confirmed using micro-indentation technique. The validation of finite element predictions with analytical values and also experimental results has proved the effectiveness of the modified Zerilli–Armstrong constitutive relation for modeling the large strain extrusion-machining process. This corroborates the ability of the modified Zerilli–Armstrong relation to simulate severe plastic deformation of various types including constrained and unconstrained machining of materials with a face-centered cubic structure.

Conflict of Interest

There are no conflicts of interest.

Data Availability Statement

The data sets generated and supporting the findings of this article are obtainable from the corresponding author upon reasonable request. The authors attest that all data for this study are included in the paper.

References

[1] Valiev, R. Z., Korznikov, A. V., and Mulyukov, R. R., 1993, "Structure and Properties of Ultrafine-Grained Materials Produced by Severe Plastic Deformation," Mater. Sci. Eng. A, **168**(2), pp. 141–148.

[2] Mishra, A., Richard, V., Grégori, F., Asaro, R. J., and Meyers, M. A., 2005, "Microstructural Evolution in Copper Processed by Severe Plastic Deformation," Mater. Sci. Eng. A, **410–411**, pp. 290–298.

[3] Ravi Shankar, M., Chandrasekar, S., Compton, W. D., and King, A. H., 2005, "Characteristics of Aluminum 6061-T6 Deformed to Large Plastic Strains by Machining," Mater. Sci. Eng. A, **410–411**, pp. 364–368.

[4] Swaminathan, S., Ravi Shankar, M., and Lee, S., Hwang, J., King, A. H., Kezar, R. F., Rao, B. C., Brown, T. L., Chandrasekar, S., Compton, W. D., and Trumble, K. P., 2005, "Large Strain Deformation and Ultra-fine Grained Materials by Machining," Mater. Sci. Eng. A, **410–411**, pp. 358–363.

[5] Moscoso, W., Ravi Shankar, M., Mann, J. B., Compton, W. D., and Chandrasekar, S., 2007, "Bulk Nanostructured Materials by Large Strain Extrusion Machining," J. Mater. Res., **22**(1), pp. 201–205.

[6] Sagapuram, D., Viswanathan, K., Mahato, A., Sundaram, N. K., M'Saoubi, R., Trumble, K. P., and Chandrasekar, S., 2016, "Geometric Flow Control of Shear Bands by Suppression of Viscous Sliding," Proc. R. Soc. A, **472**(2192), p. 20160167.

[7] Shankar, M. R., Rao, B. C., Lee, S., Chandrasekar, S., King, A. H., and Compton, W. D., 2006, "Severe Plastic Deformation (SPD) of Titanium at Near-Ambient Temperature," Acta Mater., **54**(14), pp. 3691–3700.

[8] Huang, C., Murthy, T. G., Shankar, M. R., M'Saoubi, R., and Chandrasekar, S., 2008, "Temperature Rise in Severe Plastic Deformation of Titanium at Small Strain-Rates," Scr. Mater., **58**(8), pp. 663–666.

[9] De Chiffre, L., 1976, "Extrusion-cutting," Int. J. Mach. Tool Des. Res., **16**(2), pp. 137–144.

[10] Sevier, M., Yang, H. T. Y., Moscoso, W., and Chandrasekar, S., 2008, "Analysis of Severe Plastic Deformation by Large Strain Extrusion Machining," Metall. Mater. Trans. A, **39**(11), pp. 2645–2655.

[11] Sagapuram, D., Udupa, A., Viswanathan, K., Mann, J. B., M'Saoubi, R., Sugihara, T., and Chandrasekar, S., 2020, "On the Cutting of Metals: A Mechanics Viewpoint," ASME J. Manuf. Sci. Eng., **142**(11), p. 110808.

[12] Jawahir, I. S., Schoop, J., Kaynak, Y., Balaji, A. K., Ghosh, R., and Lu, T., 2020, "Progress Toward Modeling and Optimization of Sustainable Machining Processes," ASME J. Manuf. Sci. Eng., **142**(11), p. 110811.

[13] H. K. S., 2012, "ABAQUS/Explicit Analysis User Manual," Version 6.12.

[14] Arrazola, P. J., 2010, "Investigations on the Effects of Friction Modeling in Finite Element Simulation of Machining," Int. J. Mech. Sci., **52**(1), pp. 31–42.

[15] Adibi-Sedeh, A. H., and Madhavan, V., 2003, "Understanding of Finite Element Analysis Results Under the Framework of Oxley's Machining Model," Proceedings of the Sixth CIRP International Workshop on Modeling of Machining Operations, Hamilton, Canada, May 20, pp. 1–15.

[16] Ozel, T., and Zeren, E., 2005, "Finite Element Method Simulation of Machining of AISI 1045 Steel With a Round Edge Cutting Tool," Proceedings of the Eighth CIRP International Workshop on Modeling of Machining Operations, Chemnitz, Germany, May 10–11, pp. 533–542.

[17] Gurusamy, M. M., and Rao, B. C., 2017, "On the Performance of Modified Zerilli-Armstrong Constitutive Model in Simulating the Metal-Cutting Process," J. Manuf. Processes, **28**, pp. 253–265.

[18] Olovsson, L., Nilsson, L., and Simonsson, K., 1999, "An ALE Formulation for the Solution of Two-Dimensional Metal Cutting Problems," Comput. Struct., **72**(4–5), pp. 497–507.

[19] Samantaray, D., Mandal, S., Borah, U., Bhaduri, A. K., and Sivaprasad, P. V., 2009, "A Thermo-viscoplastic Constitutive Model to Predict Elevated-Temperature Flow Behaviour in a Titanium-Modified Austenitic Stainless Steel," Mater. Sci. Eng. A, **526**(1–2), pp. 1–6.

[20] Laakso, S. V. A., 2017, "Heat Matters When Matter Heats—The Effect of Temperature-Dependent Material Properties on Metal Cutting Simulations," J. Manuf. Processes, **27**, pp. 261–275.

[21] Lee, S., Hwang, J., Shankar, M. R., Chandrasekar, S., and Compton, W. D., 2006, "Large Strain Deformation Field in Machining," Metall. Mater. Trans. A, **37**(5), pp. 1633–1643.

[22] Molafilabi, S., Sadeghi, A., and Hadad, M., 2020, "Investigation of Large Strain Extrusion Machining (LSEM) of Pure Magnesium (Mg)," Int. J. Lightweight Mater. Manuf., **3**(2), pp. 100–107.

[23] Guo, Y., Chen, J., and Saleh, A., 2020, "In situ Analysis of Deformation Mechanics of Constrained Cutting Toward Enhanced Material Removal," ASME J. Manuf. Sci. Eng., **142**(2), p. 021002. .

[24] Shi, B., 2008, "Identification of the Material Constitutive Equation for Simulation of the Metal Cutting Process," Ph.D., thesis, McGill University, Montreal, QC, Canada.

[25] Movahhedy, M., Gadala, M. S., and Altintas, Y., 2000, "Simulation of the Orthogonal Metal Cutting Process Using an Arbitrary Lagrangian–Eulerian Finite-Element Method," J. Mater. Process. Technol., **103**(2), pp. 267–275.

[26] Palaniappan, K., Murthy, H., and Rao, B. C., 2018, "Production of Fine-Grained Foils by Large Strain Extrusion-Machining of Textured Ti–6Al–4 V," J. Mater. Res., **33**(2), pp. 108–120.

[27] Merchant, M. E., 1945, "Mechanics of the Metal Cutting Process," J. Appl. Phys., **16**(5), pp. 267–275.

[28] Slama, C., Servant, C., and Cizeron, G., 1997, "Aging of the Inconel 718 Alloy Between 500 and 750 C," J. Mater. Res., **12**(9), pp. 2298–2316.